Society of Medical Education & Research

2023, Volume 3, Issue 1, Page No: 156-175
ISSN: 3108-4834

Archive of International Journal of Cancer and Allied Science

Dissecting CAF-Immune Crosstalk in H. pylori-Positive Gastric Cancer: THBS1-WNT5 Treg Recruitment and ZFP36-Mediated Suppression of Cytotoxic T-Cell Activation

Keiko Masami Ito[1]*, Yuko Akari Tanaka[1]

[1]Department of Radiation Oncology, Osaka University Hospital, Osaka, Japan.

***E-mail** ✉ k.ito.osaka@yahoo.com

Abstract

Cancer-associated fibroblasts (CAFs) play a central role in modulating the tumor microenvironment, but their spatial arrangement and immune-regulatory roles in Helicobacter pylori-related gastric cancer (GC) are still poorly characterized. Formalin-fixed paraffin-embedded (FFPE) tumor samples from 71 patients with GC were analyzed via spatial transcriptomics, with data integrated from single-cell RNA sequencing across three separate cohorts (originating from China, the United States, and Singapore). Interactions between CAFs and immune cells were assessed through neighborhood enrichment analysis and aggregation index scoring. CAF signaling pathways and developmental trajectories were elucidated using ligand-receptor prediction and pseudotime analysis. Post-transcriptional regulation was explored by integrating AU-rich element (ARE) motif detection, gene expression correlations, and laser-assisted crosslinking and immunoprecipitation sequencing (LACE-seq) to identify putative ZFP36 binding targets. The tumor immune composition and survival correlations were examined via CIBERSORT-ABS deconvolution and Kaplan-Meier survival curves in the TCGA and ACRG datasets.

The study initially mapped the spatial localization of four previously described CAF subpopulations and demonstrated that their links to immune components differed according to histological and infection-based GC classifications. In tumors positive for H. pylori, THBS1-expressing CAFs showed marked proximity to regulatory T cells (Tregs) and contributed to regional immune suppression via WNT5-FZD signaling. Concurrently, the RNA-binding protein ZFP36 targeted AU-rich elements in the FN1 3′ untranslated region (3'UTR), promoting FN1 mRNA degradation and consequently reducing the ability of $FN1^{+}$ CAFs to stimulate cytotoxic T lymphocytes (CTLs). These two mechanisms collectively enhanced Treg presence while inhibiting CTL function. The results uncover infection-driven stromal mechanisms that remodel the immune milieu in gastric cancer and identify CAF-related signaling networks as promising candidates for targeted therapy in H. pylori-linked GC.

Keywords: Gastric cancer, CAF-immune, THBS1-WNT5, Cytotoxic T-cell

Introduction

Gastric cancer (GC) represents a significant worldwide health challenge and continues to rank among the primary causes of death from malignancy globally, showing only modest survival gains despite progress in treatment [1]. The disease arises from a multifaceted interaction of hereditary, lifestyle, and infectious elements, with Helicobacter pylori (H. pylori) firmly established as a major contributor to gastric oncogenesis [2, 3]. This pathogen exerts a particularly heavy impact in Asian populations, where it displays elevated prevalence and the clearest epidemiologic connection to gastric tumor formation [4]. Through sustained inflammation, mucosal damage, and precancerous changes, H. pylori alters both stromal and immune elements, thereby compromising gastric tissue equilibrium and facilitating progression to cancer [5, 6]. From a histopathological perspective, GC is traditionally divided according to the Lauren classification into intestinal and diffuse variants, which vary in appearance, behavior, and reaction to H. pylori-triggered inflammation [7–9]. The intestinal variant shows a

Access this article online https://smerpub.com/

Received: 11 March 2023; **Accepted:** 04 June 2023

How to cite this article: Ito KM, Tanaka YA. Dissecting CAF-Immune Crosstalk in H. pylori-Positive Gastric Cancer: THBS1-WNT5 Treg Recruitment and ZFP36-Mediated Suppression of Cytotoxic T-Cell Activation. Arch Int J Cancer Allied Sci. 2023;3(1):156-75. https://doi.org/10.51847/9nfV6lOxSf

stronger link to longstanding atrophic gastritis and metaplastic changes, along with greater rates of detectable H. pylori compared to the diffuse variant [10]. In contrast, diffuse GC tends to be driven more by inherited factors and relies less on infection-related inflammatory processes. Such differences indicate distinct oncogenic pathways by subtype [11, 12], although the specific influence of H. pylori on immune profiles and molecular characteristics across these categories is not fully clarified.

A prominent outcome of H. pylori infection is prolonged stimulation of the gastric tumor immune milieu. This features extensive leukocyte recruitment and ongoing release of inflammatory mediators, which impair epithelial integrity while also influencing stromal populations, notably cancer-associated fibroblasts (CAFs) [2]. CAFs are increasingly recognized as central players in infection-associated inflammation. Experimental models have illustrated that H. pylori can convert resting fibroblasts into CAF-like states [13], and prior research from our group revealed that the bacterium enhances CAF accumulation and matrix reorganization through the NF-κB/PIEZO1/YAP1/CTGF pathway [14]. Activated CAFs produce diverse soluble factors, chemotactic signals, and matrix proteins that collectively support tumor cell growth, vessel formation, and immune escape [15–17]. In recent work, we comprehensively profiled the CAF population and defined four discrete subsets with unique transcriptional and functional properties: progenitor CAF (proCAF), inflammatory CAF (iCAF), myofibroblastic CAF (myCAF), and matrix CAF (matCAF) [18]. Although this framework underscores CAF diversity, the manner in which H. pylori modulates the proportions of these subsets and their spatial relationships with malignant cells in different GC histological types remains unresolved.

Notably, spatial transcriptomics has emerged as a transformative approach for unraveling the intricate organization of the GC tumor microenvironment (TME), permitting gene expression mapping while maintaining tissue architecture [19]. Moreover, its combination with single-cell RNA sequencing (scRNA-seq) provides detailed insights into cellular diversity, lineage progression, and cell-cell signaling [20]. Here, we applied an integrated spatial and single-cell transcriptomics methodology to thoroughly examine CAF spatial distribution across GC variants and assess how H. pylori affects CAF subset representation and immune-modulating activities, aiming to clarify CAF contributions to the immunosuppressive setting in GC.

Materials and Methods

GC patient cohorts and cell lines

The investigation utilized several GC patient datasets from varied geographical and clinical contexts to enable robust spatial and single-cell transcriptomic evaluation. Spatial transcriptomics was conducted on formalin-fixed paraffin-embedded (FFPE) tumor specimens obtained from 71 GC cases diagnosed between 1999 and 2006 at Prince of Wales Hospital in Hong Kong. The study received ethical clearance from the Joint Chinese University of Hong Kong-New Territories East Cluster Clinical Research Ethics Committee (CREC Ref. No. 2022.060). Single-cell RNA-seq datasets were sourced from three distinct GC collections. The Chinese dataset encompassed 10 patients enrolled at the Affiliated Drum Tower Hospital of Nanjing University Medical School, approved by the local ethics board [21]. The American dataset involved 22 GC samples from an earlier published resource (https://dna-discovery.stanford.edu/research/datasets/) [22]. The Singapore dataset covered 26 patients and was retrieved from the Gene Expression Omnibus repository (GSE183904) [23]. Additionally, the human gastric adenocarcinoma cell line HGC-27 was acquired from ECACC (Cat. 94,042,256), verified via short tandem repeat (STR) analysis before experiments, and confirmed mycoplasma-free through regular testing. Cells were grown in RPMI-1640 medium containing 10% fetal bovine serum and 1% penicillin-streptomycin, incubated at 37°C with 5% CO_2. HGC-27 cells were employed solely for LACE-seq procedures and were maintained under identical conditions right before UV crosslinking and sequencing library construction.

Spatial transcriptomic profiling using cosMx SMI

FFPE tissue sections from the 71 GC cases underwent spatial transcriptomic processing. Sections were affixed to CITOGLAS slides and baked overnight at 60°C to promote firm attachment. Antigen retrieval was achieved by heat treatment in ER1 buffer (Leica Biosystems) at 100°C for 15 min, succeeded by proteinase K digestion (ACD Protease Plus) for 30 min. Following rinses in DEPC-treated water, fiducial beads (Bangs Laboratories) suspended in 2 × SSCT were added for alignment reference, then washed in PBS and fixed with 10%

neutral-buffered formalin. Subsequent washes involved Tris-glycine and PBS, followed by blocking with 100 mM NHS-acetate at room temperature and rinsing in 2 × SSC. A SecureSeal chamber (Grace Bio-Labs) was affixed to each slide.

After short denaturation at 95°C, overnight hybridization at 37°C was carried out with a probe panel consisting of 980-plex and tailored in situ hybridization probes (NanoString), along with attenuation probes, buffer R, and SUPERase·In. Following hybridization, slides underwent serial washes in 2 × SSCT, 50% formamide/2 × SSC at 37°C, and 2 × SSC at ambient temperature. Slides were re-blocked and readied for analysis on the CosMx™ Spatial Molecular Imager (NanoString Technologies). Fields of view (FOVs; 0.51 × 0.51 mm) were chosen using H&E-guided reference images. Reporter probes were loaded into the flow cell, incubated, washed, and imaged. Z-stack imaging across nine layers at 0.8 μm steps was performed per FOV. For protein-level spatial mapping, sections received fluorophore-labeled antibodies targeting PanCK, CK8/18, CD45, membrane markers, and nuclear stains, followed by multi-channel fluorescent capture. Raw images were analyzed via the AtoMx Spatial Informatics Platform for subsequent interpretation.

Image processing and spatial transcript assignment

Advanced image analysis was conducted to delineate individual cells and map RNA transcripts to their precise locations in tissue [24]. Cell membranes and boundaries were detected employing multilayer immunofluorescence stacks, incorporating nuclear (DAPI) staining and membrane markers, via deep learning-driven segmentation tools. Identified transcripts were subsequently allocated to specific cells and their intracellular regions, allowing the assembly of gene expression profiles at the resolution of single cells. For effective display, transcript locations were superimposed on outlined cell shapes using the napari viewer. Different channels of immunofluorescence were assigned unique false colors, and brightness adjustments were applied to create merged images highlighting RNA distribution alongside histological structures.

ScRNA-seq data processing

Single-cell RNA sequencing datasets were handled in Python (version 3.8). The three publicly available single-cell collections were combined using the "anndata.concat" function. Low-quality or damaged cells were filtered out by removing those with less than 500 counts, fewer than 200 unique genes detected, or mitochondrial transcript proportions above 20%. Further processing steps were executed with Scanpy (version 1.9.6). Count data were normalized and standardized by applying "scanpy.preprocessing.normalize_total" and "scanpy.preprocessing.scale". Batch correction across different samples was achieved through the Harmony algorithm.

Cell type annotation

Data dimensionality was reduced via principal component analysis (PCA), succeeded by community detection clustering using "scanpy.tools.leiden" and embedding visualization with "scanpy.tools.umap". UMAP projections served as the primary visualization method. Marker gene identification was performed with "scanpy.tools.rank_gene_groups", and cellular identities were determined according to established signature genes and reference transcriptional profiles from prior literature.

Neighborhood enrichment analysis

Spatial co-occurrence patterns among various cell populations were assessed through neighborhood enrichment evaluation, leveraging positional data and cell-type labels obtained from CosMx SMI outputs. For every cell, the composition of adjacent cell types within a specified radius was measured. Statistical significance was determined by comparing actual frequencies to a null model created via repeated random reassignment of cell-type labels while preserving positions. Enrichment values were expressed as logarithmized ratios of observed to expected occurrences. Results were presented in dot plot format, where color depth indicated the magnitude of enrichment and circle diameter reflected p-value thresholds. This approach revealed selective spatial associations between CAF subpopulations and nearby cellular communities.

Spatial aggregation index (SAI) score calculation

A custom distance-weighted SAI metric was implemented to measure spatial proximity between selected cell populations, incorporating local neighborhood content and intercellular distances. Cell positions were retrieved from the AnnData structure (adata.obsm['spatial']). For each focal cell i, the t closest neighbors were found using Euclidean distance (NearestNeighbors). Within this local environment, cells

belonging to center or target categories were marked, and the following parameters were calculated: (a) overall count of center cells in the sample; (b) overall count of target cells in the sample; (c) count of center cells in the neighborhood; (d) count of target cells in the neighborhood; (e) average Euclidean distance between paired center and target cells locally. The inverse of this average distance served as a proximity penalty weight. The SAI score was formulated as:

where T represents total cells, t denotes neighbor count, and di indicates average center-target distance in the neighborhood of cell i. Neighborhoods lacking center-target interactions received an SAI of zero. Computed SAI values were added to cell metadata (adata.obs) for further plotting and statistical testing. Specifically, calculations used n_neighbors = 30, with results stored in adata.obs. Enrichment outcomes were displayed via (i) dot plots combining color and size for strength representation, and (ii) tissue-based scatter plots using color gradients for enrichment levels.

Trajectory inference

Cellular differentiation paths and pseudotime ordering were modeled using the Palantir package (version 1.4.1) on the single-cell dataset [25]. Following normalization and PCA-based reduction, the leading components informed the construction of a diffusion map to reflect the underlying manifold structure. An initial cell was selected according to high expression of established stem or precursor markers. Palantir generated pseudotime assignments and fate probabilities for all cells. The inferred trajectory illustrated continuous state transitions and branching toward terminal lineages. Temporal gene dynamics were fitted with generalized additive models (GAMs), and key trajectory-related genes were depicted in heatmaps and smoothed expression curves.

Integration of scRNA-seq with spatial transcriptomics

The Tangram framework (version 1.0.4) was utilized to align single-cell RNA-seq profiles with spatial transcriptomic data. Preprocessing was initiated via the pp_adatas function, followed by cell-to-space projection using map_cells_to_space for deconvolution. These alignments facilitated the prediction of cell-type distributions and organizational patterns across the tissue sections.

Kaplan–meier survival analysis

Survival outcomes were assessed via Kaplan-Meier estimation using the lifelines package (version 0.27.8) to examine links between patient prognosis and levels of ZFP36 and THBS1 expression, as well as Spatial Aggregation Index (SAI) values for immune cells. Cases were divided into high and low groups using the median as the cutoff for either gene expression or SAI score. Survival curves were generated with KaplanMeierFitter, and group differences were tested statistically through the log-rank method. Clinical and transcriptomic information for gastric cancer patients was sourced from the TCGA and ACRG datasets [11, 26].

Gene set scoring and spatial association analysis

To explore the immune-modulating capacity of $THBS1^+$ CAFs, two publicly available gene sets were retrieved from MSigDB: GSE7460_TREG_VS_TCONV_ACT_UP and GSE25087_TREG_VS_TCONV_ADULT_UP. Enrichment scores for these sets were computed at each spatial location using the AUCell method. $THBS1^+$ CAFs were identified by applying a predefined expression cutoff for THBS1. Spatial proximity was measured with the Spatial Aggregation Index (SAI) and displayed on tissue coordinates to evaluate possible functional links between THBS1 levels and Treg-associated regulatory activity.

Cell-cell communication analysis

Intercellular signaling networks were inferred with the CellChat package in R (version 2.1.0), which relies on a comprehensive ligand-receptor database. Signaling strengths between cell populations were calculated via the “computeCommunProb” function, followed by removal of weak interactions using “filterCommunication”. Pathway-specific signaling intensities were derived with “computeCommunProbPathway”, and global network summaries were produced through the “aggregateNet” function.

GO enrichment analysis

Differential gene expression was identified using the “scanpy.tools.rank_gene_groups” function in Scanpy (version 1.9.6), employing the Wilcoxon rank-sum test with Bonferroni adjustment. Genes were deemed significant if adjusted $P < 0.05$ and $\log_2$ fold change ($\log_2FC$) > 0.2. For certain comparisons, a less stringent criterion was applied ($\log_2FC > 0.1$ and $P < 0.05$).

Functional enrichment of the selected gene lists was performed via Metascape [27].

Laser-assisted crosslinking and immunoprecipitation sequencing (LACE-seq)

LACE-seq was carried out to detect RNA molecules bound by the RNA-binding protein ZFP36. In brief, cells underwent UV irradiation to stabilize protein-RNA complexes, after which ZFP36 was immunoprecipitated with a specific antibody. Captured RNA fragments were isolated, reverse-transcribed into libraries, and sequenced at high depth. Sequencing reads were mapped to the human genome (hg38) with bowtie (version 2.5.4). Enrichment peaks were identified using Piranha (version 1.2.1) to pinpoint reliable crosslinking positions. Peaks were annotated to transcript regions based on GENCODE version 42, and putative binding locations within the FN1 transcript were isolated for further examination. Peak tracks were plotted using matplotlib (version 3.5.2).

Motif scanning

Potential ZFP36-mediated post-transcriptional regulation in CAFs was investigated by combining motif detection with expression correlation analysis. Canonical AU-rich elements ("AUUUA" in RNA sequences; "ATTTA" in DNA contexts) were searched across the 3′ UTRs of all protein-coding genes from GENCODE v42 (hg38 assembly). Genes harboring at least five such motifs were flagged as possible ZFP36 targets. Separately, Pearson correlations were calculated between ZFP36 and all other genes within CAF populations from single-cell data. Genes with strongly negative correlations (Pearson's $r < -0.2$) were retained. Overlap between motif-positive and negatively correlated genes underwent false discovery rate correction (Benjamini-Hochberg), yielding a stringent target list (FDR < 0.05). Overlaps were illustrated through scatter plots integrating correlation and motif counts.

CIBERSORT analysis

Tumor-infiltrating immune cell fractions were deconvoluted using CIBERSORT-ABS (absolute mode; 1,000 permutations) on bulk expression profiles from the TCGA STAD cohort. A standard immune reference matrix was applied to estimate abundances of distinct leukocyte subsets. Associations between immune composition and fibroblast markers were explored via Pearson correlation between inferred cell proportions and key CAF-related genes.

TF network inference

Transcription factor regulatory networks were reconstructed at single-cell resolution with the pySCENIC workflow (version 0.12.1). TF-target links were derived from co-expression patterns and cis-regulatory motif scanning, using GRNBoost2 for inference and motif data from the Cistrome resource. Promoter regions were defined as 500 bp upstream to 100 bp downstream of transcription start sites on hg38. Robust regulons were kept after adjustment ($P < 0.01$). Regulon activity per cell was scored with AUCell, producing a comprehensive activity matrix. For display, these scores were overlaid on UMAP embeddings via matplotlib (version 3.5.2), with color gradients indicating activity strength.

Statistical analysis

All statistical tests were performed using the "scipy.stats" module. For comparisons between two groups, Student's t-test was applied when data met assumptions of normality and equal variances; Welch's t-test was used for unequal variances. Non-parametric alternatives were employed via the Mann-Whitney U test when assumptions were violated. Tests were two-sided except where specified otherwise. Precise P values are provided in figures and text, with statistical significance defined at $P < 0.05$.

Results and Discussion

Gastric cancer subtypes display unique spatial architectures, cellular distributions, and immune profiles

To generate a high-resolution map of the gastric cancer tumor microenvironment (TME), we combined single-cell RNA sequencing with spatial transcriptomics on human tumor specimens. The analytical pipeline enabled detailed examination of cellular diversity, positional patterns, intercellular signaling, and differentiation paths in the TME. Core methodologies encompassed neighborhood enrichment evaluation, ligand-receptor prediction, pseudotime modeling, spatial cell-type mapping, and pathway annotation **(Figure 1a)**. In this work, Helicobacter pylori infection altered the immune landscape of gastric cancer through transcriptional reprogramming of cancer-associated fibroblasts (CAFs). A THBS1-expressing CAF population clustered near

regulatory T cells (Tregs) and appeared to facilitate Treg accumulation via WNT5-FZD receptor interactions. Simultaneously, the RNA-binding protein ZFP36 recognized AU-rich elements (AUUUA) in the FN1 3′ untranslated region, accelerating FN1 mRNA decay and likely impairing cytotoxic T lymphocyte (CTL) function. Consequently, the THBS1-WNT5 pathway supporting Treg persistence and the ZFP36-FN1 pathway limiting CTL activity may synergize to establish regional immunosuppression in H. pylori-positive tumors, highlighting a potential stromal target to counteract immune escape **(Figure 1b)**.

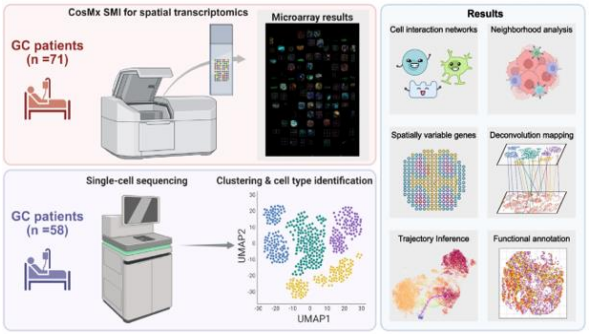

a)

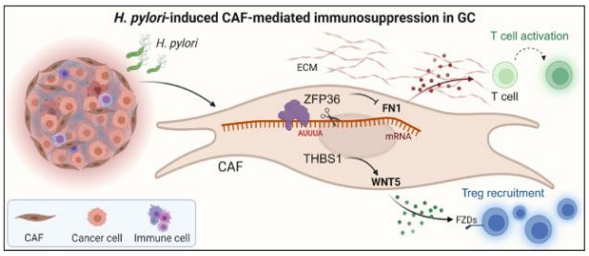

b)

Figure 1. Overview diagram of CAF-driven immune modulation in Helicobacter pylori-linked gastric cancer. **a** Illustration of the multi-omics integration strategy employed here. Single-cell and spatial transcriptomics were merged to resolve CAF diversity, tissue positioning, signaling networks, lineage progression, and functional properties in the TME. Principal techniques involved neighborhood analysis, communication inference, trajectory reconstruction, deconvolution mapping, detection of spatially variable genes, and enrichment studies. **b** Conceptual summary. Different CAF populations regulate immunity through distinct mechanisms: THBS1^{+} CAFs enhance Treg recruitment and maintenance via THBS1-WNT5 signaling, whereas ZFP36-expressing CAFs reduce cytotoxic responses by suppressing FN1 expression, together promoting an immunosuppressive ("cold") tumor milieu.

Using established marker genes, cell-type assignment in the spatial dataset delineated primary immune, stromal, and epithelial compartments, comprising T cells, B cells, dendritic cells, myeloid cells, endothelial cells, fibroblasts, smooth muscle cells, and malignant epithelial cells **(Figures 2a and 2b)**. Pronounced subtype-specific variations emerged in cellular proportions and spatial configurations across Lauren-classified gastric cancers. Intestinal-type tumors featured tightly packed malignant epithelial regions, with CAFs and immune populations concentrated along invasive fronts, yielding sharp tumor-stroma interfaces. Diffuse-type tumors, however, exhibited diffuse intermingling of cancer cells, fibroblasts, and leukocytes, producing poorly structured tissue patterns. Notably, intestinal-type specimens harbored greater immune cell fractions relative to diffuse-type cases **(Figures 2c and 2d)**.

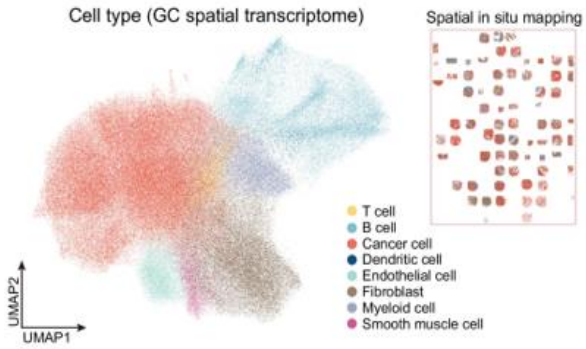

a)

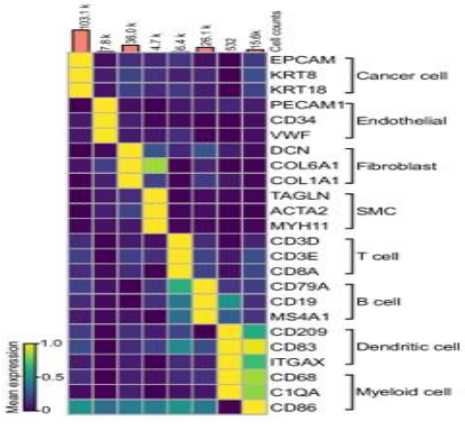

b)

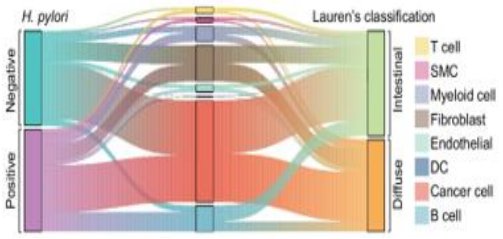

c)

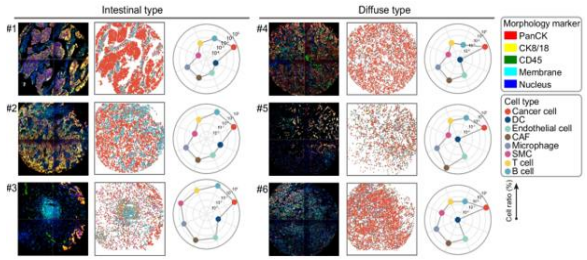

d)

Figure 2. Spatial transcriptomics uncovers cell-type distributions and histology-dependent features in gastric cancer. a UMAP embedding of spatial spots, colored according to assigned cell identities (T cells, B cells, malignant cells, dendritic cells, endothelial cells, fibroblasts, myeloid cells, smooth muscle cells). b Heatmap displaying signature marker gene expression for defining major populations in the spatial data. c Sankey diagram depicting cell-type proportions stratified by Lauren subtype (intestinal versus diffuse) and H. pylori status (positive versus negative). d Example spatial tissue maps with accompanying quantifications of cell-type abundances in intestinal- and diffuse-type tumors. Radar plots aggregate relative cell frequencies across patient samples.

To determine whether stromal-immune signaling varied by histological subtype, we conducted intercellular communication inference. Intestinal-type tumors demonstrated more organized and polarized interaction patterns. By comparison, diffuse-type cases revealed intensified but scattered signaling, especially among fibroblasts, T cells, and myeloid populations. Additionally, diffuse tumors showed diminished dendritic cell outgoing signals and weaker overall T-cell networks relative to intestinal cases. These patterns imply greater antigen presentation capacity in intestinal-type tumors but constrained immune crosstalk in diffuse-type. Ligand-receptor pair analysis further confirmed reduced T-cell engagement in diffuse versus intestinal tumors. Overall, these observations highlight histology-driven differences in spatial architecture and communication networks within gastric cancer.

CAFs consist of four distinct functional subpopulations with unique spatial localization patterns

To examine the spatial diversity of cancer-associated fibroblasts (CAFs) in gastric cancer (GC), we utilized the subtype framework developed earlier from our multi-cancer single-cell resource [18]. This approach enabled mapping of four CAF populations in spatial data: proCAFs, iCAFs, matCAFs, and myCAFs **(Figures 3a and 3b)**. The assignment combined transcriptional signatures with positional information. Each subpopulation occupied preferential regions within tissue samples, indicating compartmentalized roles in the tumor ecosystem. Neighborhood enrichment evaluation disclosed population-specific proximity to malignant cells. Notably, iCAFs demonstrated the closest positioning to tumor cells **(Figure 3c)**. This observation was corroborated by distance-weighted spatial aggregation index (SAI) quantification, which ranked iCAFs highest in proximity to cancer cells, followed by myCAFs and matCAFs, while proCAFs exhibited the weakest association **(Figures 3d and 3e)**.

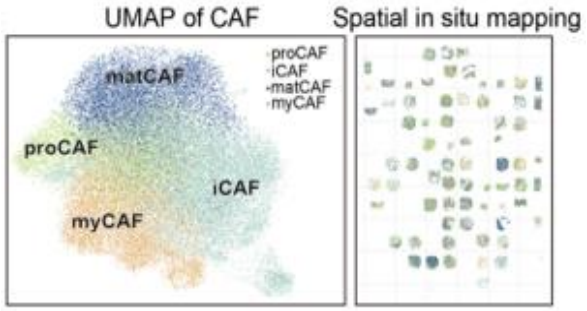

a)

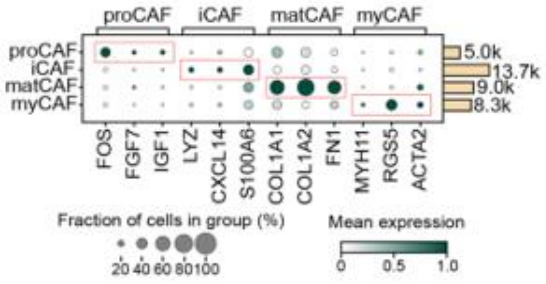

b)

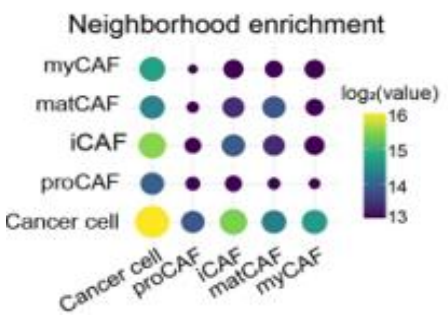

c)

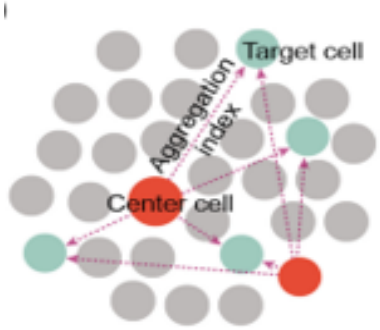

d)

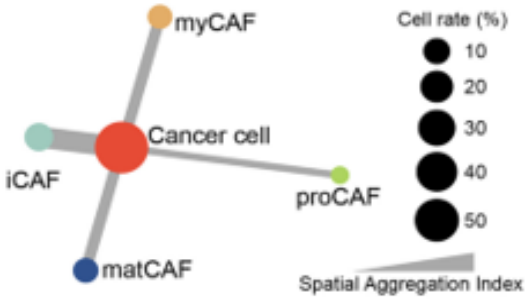

e)

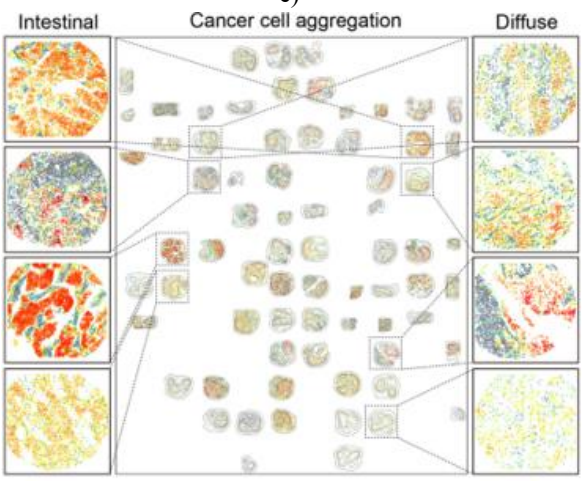

f)

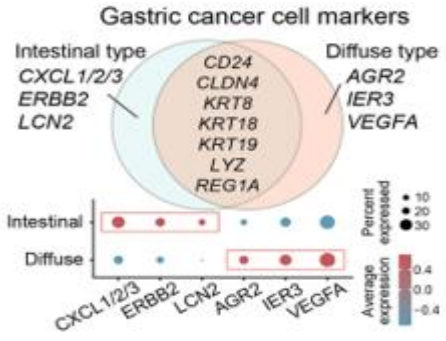

g)

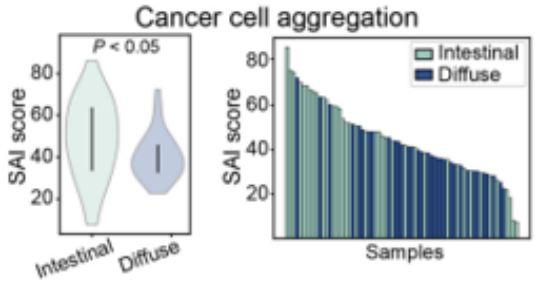

h)

Figure 3. Spatial profiling of CAF subpopulations and their proximity to malignant cells in gastric cancer. a UMAP embedding of spatial spots colored by the four CAF subpopulations: proCAF, myCAF, iCAF, and matCAF. Accompanying tissue maps depict the distribution of these subpopulations. b Dot plot illustrating key marker gene expression for distinguishing each CAF subpopulation. c Neighborhood enrichment results depicting spatial associations between CAF subpopulations and malignant cells. d Illustrative overview of the aggregation index methodology for assessing cell-type proximity. e SAI values measuring spatial aggregation strength between cancer cells and individual CAF subpopulations. f Tissue-wide views of malignant cell arrangement in various GC cases. Selected images highlight differences in cancer cell spatial patterns by histological subtype. g Expression of discriminative marker genes separating intestinal-type from diffuse-type malignant cells. h Aggregation index comparison of cancer cell clustering intensity between intestinal and diffuse subtypes.

Furthermore, SAI metrics were applied to evaluate malignant cell clustering stratified by Lauren classification. In situ spatial visualization showed clear histological differences: intestinal-type cases presented dense epithelial aggregates, whereas diffuse-type cases

featured scattered cell arrangements. These configurations aligned with divergent stromal patterns and CAF-malignant cell relationships **(Figure 3f)**. Differential marker analysis validated the molecular separation of intestinal versus diffuse malignant populations **(Figure 3g)**. SAI calculations revealed markedly elevated clustering of tumor cells in intestinal-type compared to diffuse-type tumors ($P < 0.05$;**(Figure 3h)**). Collectively, these results underscore profound differences in cellular organization and stromal interactions between GC subtypes, implying histology-dependent CAF-tumor crosstalk. Such observations motivated a deeper exploration of CAF lineage origins and governing regulatory networks.

Single-cell transcriptomics uncovers lineage trajectories and molecular signatures of CAF subpopulations

To achieve higher-resolution insight into positionally relevant transcriptional programs, we merged three independent single-cell RNA-seq collections from gastric cancer, totaling 58 cases across China, the United States, and Singapore. The combined resource encompassed over 250,000 cells. Cell-type labeling was performed using established marker genes. UMAP embeddings, supported by signature expression, delineated principal compartments: malignant cells, T cells, B cells, dendritic cells, myeloid cells, endothelial cells, fibroblasts, and smooth muscle cells **(Figures 4a and 4b)**. Within fibroblasts, the predominant fraction segregated into four CAF subpopulations—proCAFs, iCAFs, matCAFs, and myCAFs—with a small portion corresponding to normal fibroblasts. Subtype-specific markers were robustly detected across all three geographic cohorts **(Figures 4c-4e)**. Trajectory reconstruction via pseudotime placed proCAFs at an early progenitor-like position, from which three separate lineages branched toward iCAFs, matCAFs, and myCAFs, suggesting diversified differentiation paths and specialized functions **(Figure 4f)**. Comparative transcriptional profiling across pairs of subpopulations highlighted extensive molecular divergence, reinforcing their distinct identities and functional specialization **(Figure 4g)**.

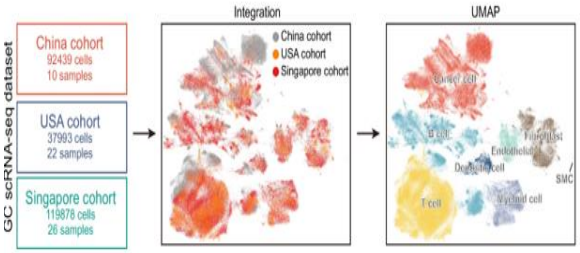

a)

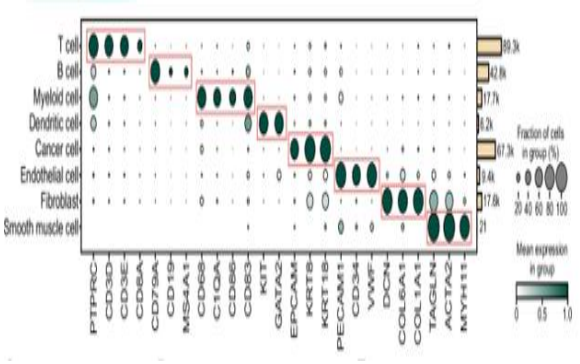

b)

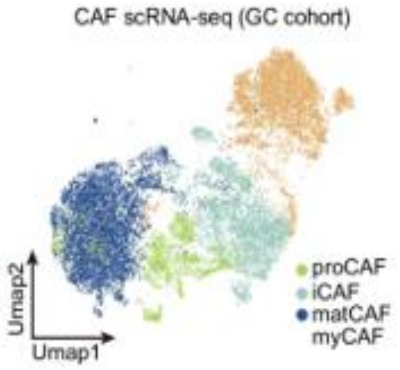

c)

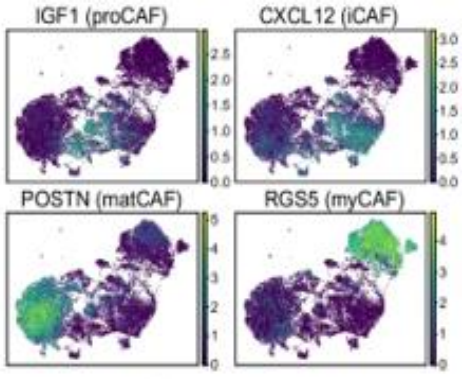

d)

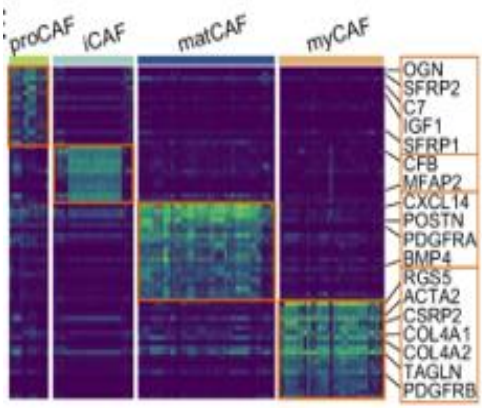

e)

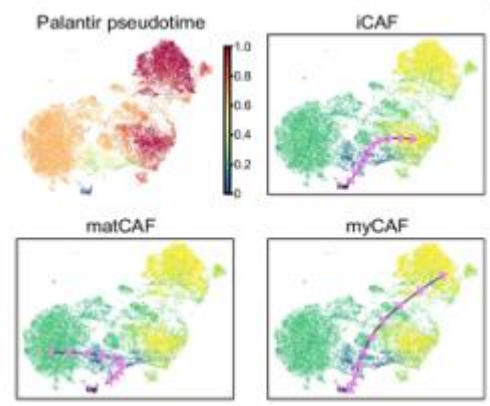

f)

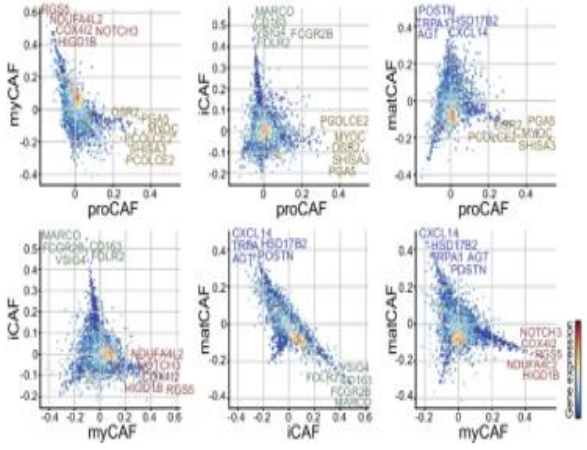

g)

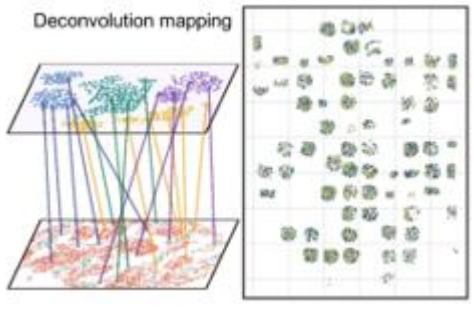

h)

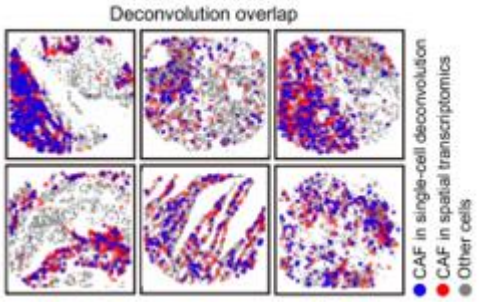

i)

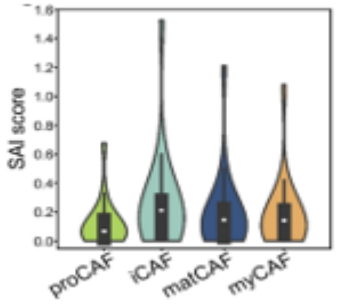

j)

Figure 4. Single-cell RNA-seq characterization of CAF subpopulations and their positional features in gastric cancer. **a** UMAP representation of integrated gastric cancer samples from three geographic sources (China, USA, Singapore), displaying overall cellular diversity. **b** Dot plot of standard marker gene expression defining primary cell categories in the merged single-cell dataset. **c** UMAP projection highlighting the four CAF subpopulations resolved from integrated single-cell data: proCAF, myCAF, iCAF, and matCAF. **d** Feature plots on UMAP showing the distribution of selected marker genes for each CAF subpopulation. **e** Heatmap of signature marker expression across identified CAF subpopulations from scRNA-seq. **f** Pseudotime-based lineage inference for CAFs, illustrating probable developmental progression among subpopulations. **g**

Inter-subpopulation differential gene comparisons, with individual dots corresponding to genes. **h** Deconvolution mapping of single-cell-derived cell identities onto spatial transcriptomic coordinates. Left: conceptual diagram of profile transfer from scRNA-seq to tissue positions; Right: resulting spatial patterns of predicted cell types. **i** Overlay images comparing spatial locations of deconvoluted CAFs (blue) versus directly detected CAFs from spatial data (red). Grey indicates non-CAF cells. **j** SAI metrics evaluating spatial aggregation between each CAF subpopulation and malignant cells.

To connect these transcriptional profiles with tissue positioning, we mapped single-cell-derived cell identities onto spatial transcriptomic datasets through deconvolution, allowing visualization of CAF and other major population distributions across the tissue. The predicted positional patterns aligned closely with those obtained from native spatial clustering **(Figures 4h and 4i)**, confirming reliability in subtype placement. Deconvolution-based evaluation of CAF subpopulation proximity to malignant cells reaffirmed the highest aggregation of iCAFs with tumor cells and the lowest for proCAFs, consistent with earlier evidence of iCAFs occupying the nearest positions to cancer cells **(Figure 4j)**. Overall, these observations indicate that CAF subpopulations vary in both developmental maturity and gene regulation alongside their distinct spatial arrangements, revealing integrated molecular and positional diversity in the tumor microenvironment.

Helicobacter pylori infection alters CAF proportions and upregulates THBS1 and ZFP36 in gastric cancer

A key issue is whether H. pylori infection modifies the stromal compartment in gastric cancer (GC), and equally critical is understanding its effects on CAF subset representation and transcriptional control. To explore this, we compared spatial transcriptomic profiles between H. pylori-positive and H. pylori-negative tumors. Tissue mapping showed markedly elevated CAF fractions in infected cases **(Figure 5a)**. Differential expression screening pinpointed THBS1 and ZFP36 as the most strongly induced genes in positive samples. Single-cell sequencing validated predominant fibroblast expression of both genes **(Figures 5b and 5c)**. At the subpopulation level, THBS1 was mainly enriched in matCAFs, while ZFP36 showed a preference for proCAFs. Spatial data consistently displayed elevated THBS1 and ZFP36 signals in infected tumors, corroborated by UMAP projections and violin distributions **(Figures 5d and 5e)**. These patterns were independently replicated in the ACRG dataset **(Figure 5f)**.

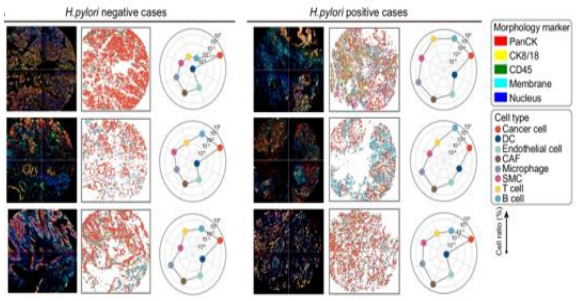

a)

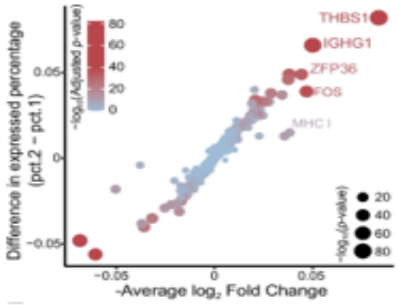

b)

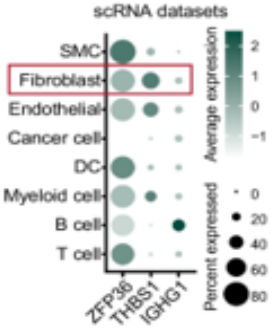

c)

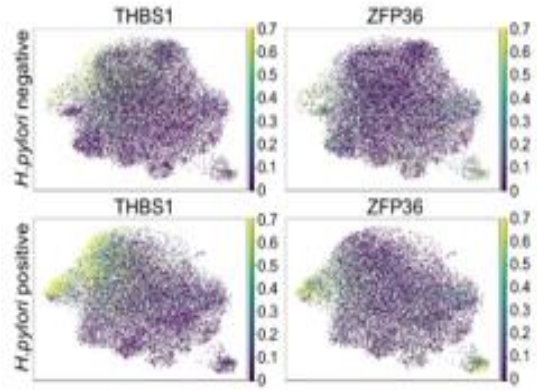

d)

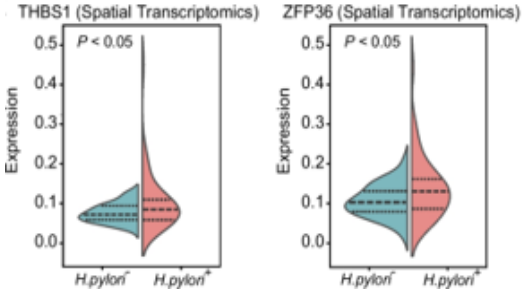

e)

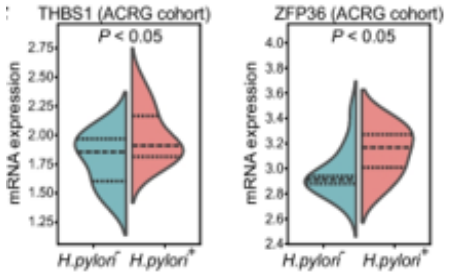

f)

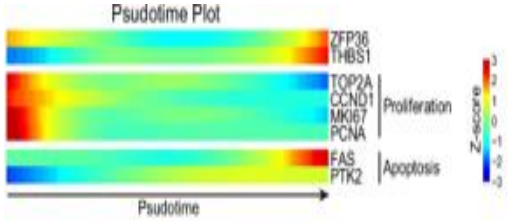

g)

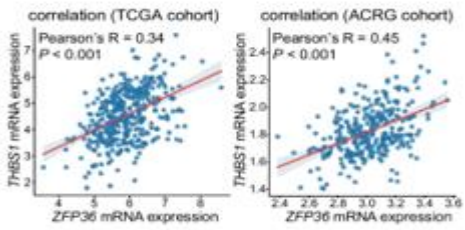

h)

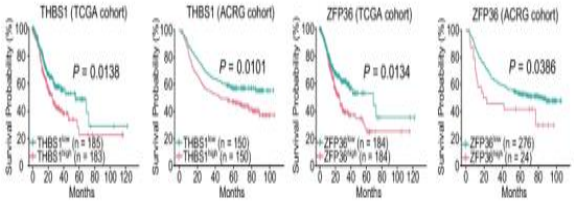

i)

Figure 5. Expression patterns and survival associations of THBS1 and ZFP36 in H. pylori-linked gastric cancer. **a** Example spatial visualizations and cell-type proportion quantifications in H. pylori-positive versus negative tumors. Radar plots aggregate relative cell abundances per sample from spatial annotations. **b** Bubble chart of genes differentially expressed between infection statuses, marking prominent upregulated genes in the negative group. **c** Distribution of selected gene expression (THBS1, ZFP36, IGHG1) across cellular compartments in single-cell data. **d** UMAP overlays of THBS1 and ZFP36 levels in CAFs stratified by H. pylori status. **e** Violin comparisons of THBS1 and ZFP36 expression in CAFs from spatial transcriptomics by infection group. **f** Violin displays of THBS1 and ZFP36 mRNA in H. pylori-positive versus negative cases from the ACRG collection. **g** Pseudotime trends of ZFP36, THBS1, and selected proliferation/apoptosis genes along CAF lineage progression, shown as Z-scored values. **h** Correlation plots between THBS1 and ZFP36 transcript levels in TCGA and ACRG gastric cancer datasets. **i** Kaplan-Meier plots of overall survival stratified by high versus low THBS1 or ZFP36 expression in TCGA and ACRG cohorts.

Further assessment of gene dynamics during fibroblast maturation via pseudotime revealed progressive upregulation of THBS1 and ZFP36 toward mature states, coinciding with activation of apoptosis regulators like FAS and PTK2 **(Figure 5g)**. Cross-dataset correlation confirmed robust positive linkage between THBS1 and ZFP36 expression in both TCGA and ACRG cohorts **(Figure 5h)**. Prognostic evaluation indicated that elevated levels of either gene correlated with significantly worse overall survival **(Figure 5i)**. In summary, H. pylori infection promotes CAF expansion and triggers enhanced transcription of THBS1 and ZFP36, particularly within the proCAF population.

THBS1-expressing CAFs facilitate Treg accumulation and immunosuppression through WNT5-FZD ligand-receptor signaling

To assess the immune-modulatory contribution of THBS1⁺ CAFs in H. pylori-positive gastric cancer, we segregated CAFs by THBS1 levels in spatial transcriptomic profiles. This yielded separate THBS1⁺ and THBS1⁻ groups with clear expression divergence **(Figures 6a and 6b)**. Notably, THBS1⁺ CAFs showed enrichment for Treg-related pathways, such as FOXP3/TGF-β networks and CD4⁺ T-cell regulatory circuits **(Figure 6c)**. T-cell heterogeneity was resolved into six spatially mapped clusters: cytotoxic T lymphocytes (CTLs), regulatory T cells (Tregs), Th1, Th2, Th17, and proliferating T cells **(Figures 6d and 6e)**. Spatial aggregation index evaluation highlighted pronounced proximity between Tregs and THBS1⁺ CAFs **(Figure 6f)**. High Treg clustering near THBS1⁺ CAFs corresponded to poorer patient survival **(Figure 6g)**. Illustrative tissue views underscored this positional linkage **(Figure 6h)**. Integration of established Treg signatures (GSE25087 and GSE7460) demonstrated partial spatial overlap between Treg pathway activity and THBS1⁺ CAF regions **(Figure 6i)**. Intercellular signaling inference identified enriched ligand-receptor pairs linking THBS1⁺ CAFs to Tregs, with WNT5A-FZD6 and WNT5B-FZD5 emerging as dominant pathways **(Figures 6j-6l)**. Collectively, these data reveal that THBS1⁺ CAFs cluster with Tregs and mediate WNT5-FZD interactions, thereby fostering localized immune suppression in H. pylori-driven gastric cancer.

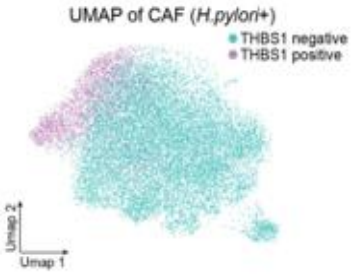

a)

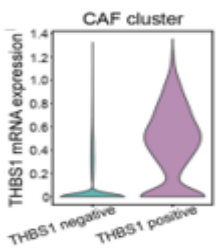

b)

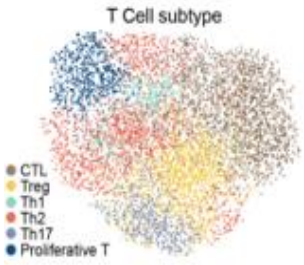

d)

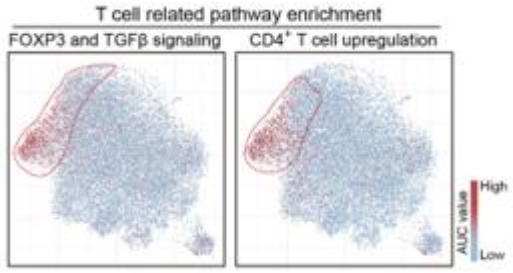

c)

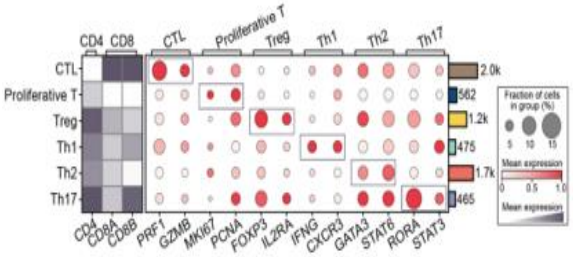

e)

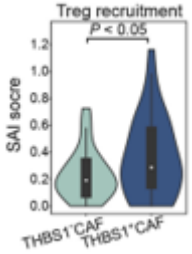

f)

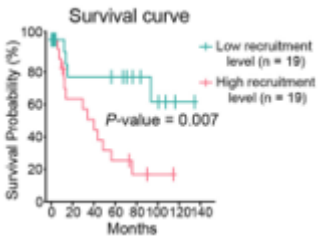

g)

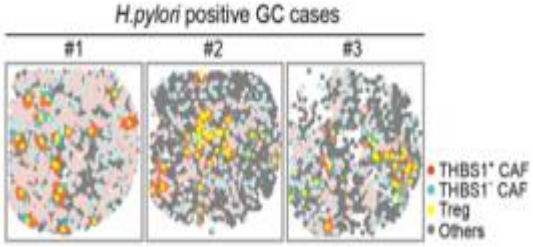

h)

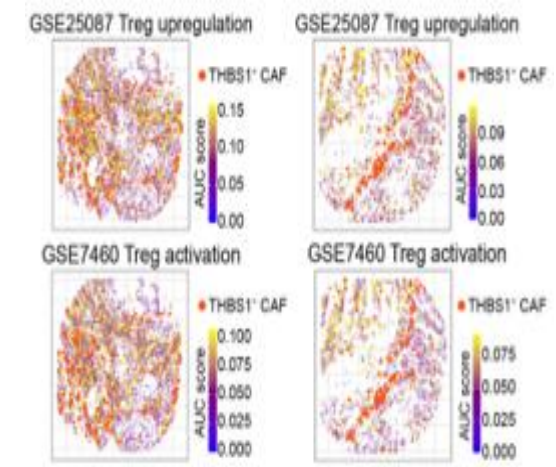

i)

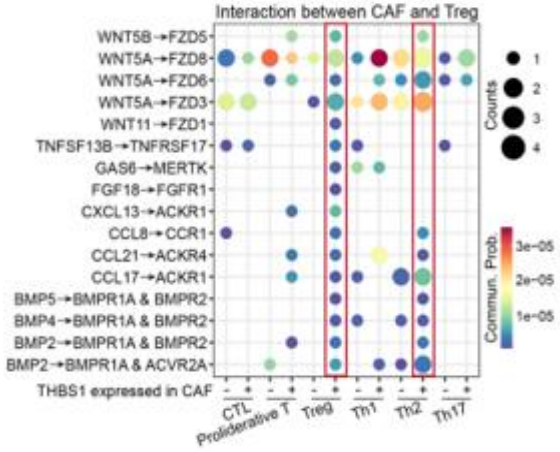

j)

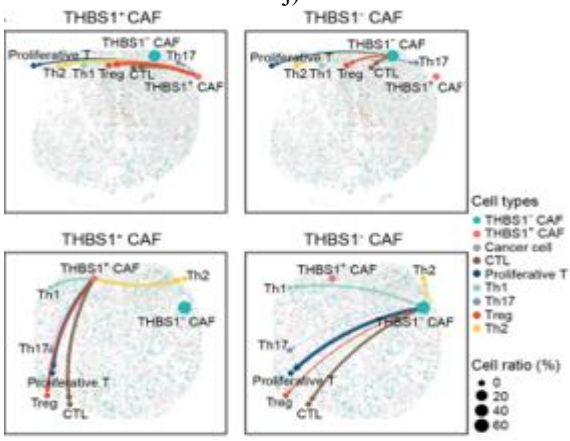

k)

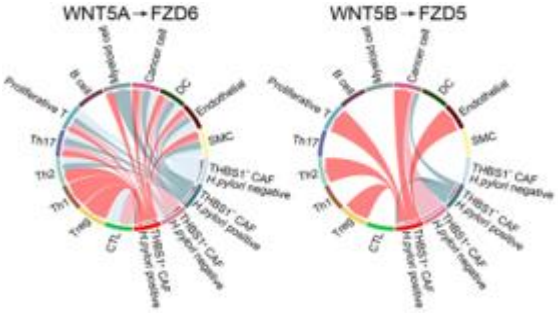

l)

Figure 6. THBS1-expressing CAFs facilitate Treg accumulation and immunosuppression in Helicobacter pylori-linked gastric cancer. **a** UMAP embedding distinguishing THBS1$^+$ and THBS1$^-$ CAF populations was resolved from spatial transcriptomic profiles. **b** Violin distribution confirming separation of THBS1$^+$ versus THBS1$^-$ CAF groups by THBS1 transcript levels. **c** Pathway enrichment mapping of T-cell regulatory networks (FOXP3/TGF-β circuits and CD4$^+$ T-cell activation) within CAF compartments, revealing focal enrichment zones. **d** UMAP projection of resolved T-cell subpopulations in spatial data. **e** Dot plot of signature marker expression defining key T-cell categories, encompassing CTL, Treg, Th1, Th2, Th17, and proliferating T cells. The accompanying heatmap displays CD4, CD8A, and CD8B levels to support subset assignment. **f** Spatial aggregation index values comparing the proximity of THBS1$^+$ and THBS1$^-$ CAFs to adjacent Treg populations. **g** Kaplan-Meier overall survival comparison between cases with low versus high Treg clustering around THBS1$^+$ CAFs. H Tissue spatial visualizations depicting positional patterns of THBS1$^+$ CAFs, THBS1$^-$ CAFs, Tregs, and remaining cell types in **h**. pylori-positive tumors. **i** Spatial mapping of Treg activation and upregulation signatures from GSE25087 and GSE7460 datasets, indicating regions overlapping with THBS1$^+$ CAF distribution. **j** Dot plot of inferred ligand-receptor pairs linking THBS1$^+$ CAFs to various T-cell subpopulations, where circle diameter reflects interaction count and color denotes signaling probability. **k** Tissue-specific intercellular signaling diagrams showing predicted connections between THBS1$^+$ or THBS1$^-$ CAFs and T-cell groups in selected tumor sections. Arc width and hue represent estimated interaction intensity; node size corresponds to population frequency. **l** Chord plots illustrating

anticipated WNT5A-FZD6 and WNT5B-FZD5 signaling links involving THBS1⁺ or THBS1⁻ CAFs and other cellular components.

ZFP36 impairs FN1-expressing CAF-driven cytotoxic T-cell stimulation through post-transcriptional destabilization

Beyond mechanisms tied to Treg accumulation, we explored whether alternative CAF populations activate separate immune-regulatory circuits. Accordingly, we screened for transcriptional controllers of CAF genes and prioritized ZFP36, an RNA-binding protein recognized for promoting mRNA decay by targeting AU-rich elements (AREs), especially AUUUA sequences, in 3′ untranslated regions (3'UTRs) **(Figure 7a)**. Correlation screening in CAFs yielded 735 putative targets exhibiting both inverse association with ZFP36 levels (Pearson's R < -0.2) and harboring at least 5 ATTTA motifs (DNA counterparts of classic AUUUA AREs) **(Figure 7b)**. Functional enrichment indicated dominance of immune-associated processes among these candidates **(Figure 7c)**. Spatial expression overlays revealed divergent patterns for ZFP36 alongside key immunomodulatory transcripts, such as FN1, FAP, INHBA, COL10A1, and STC1 **(Figure 7d)**. FN1 emerged with the most robust inverse relationship to ZFP36 and consistently topped target rankings **(Figure 7e)**. Direct ZFP36 engagement with the FN1 3′UTR was evidenced by LACE-seq profiles from four separate experiments **(Figure 7f)**.

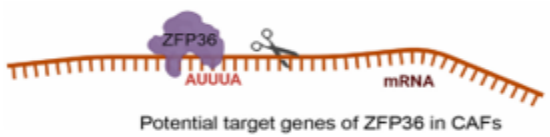

a)

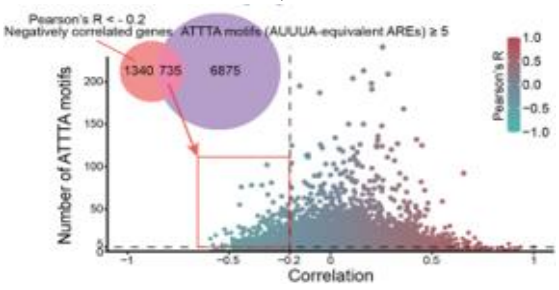

b)

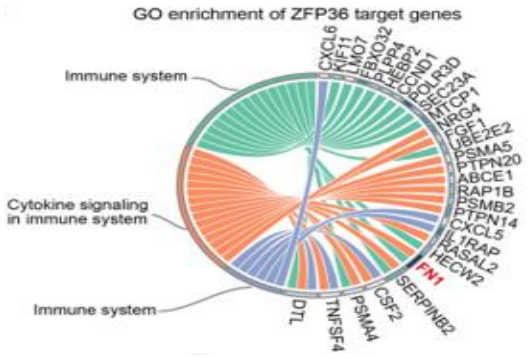

c)

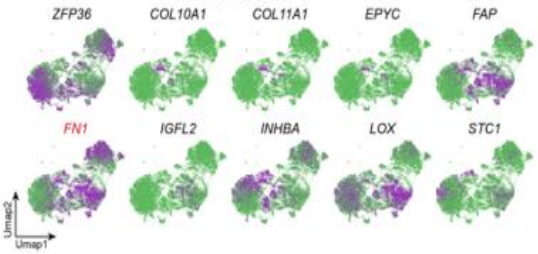

d)

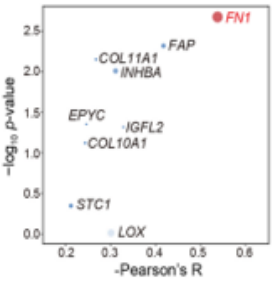

e)

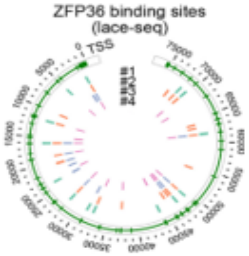

f)

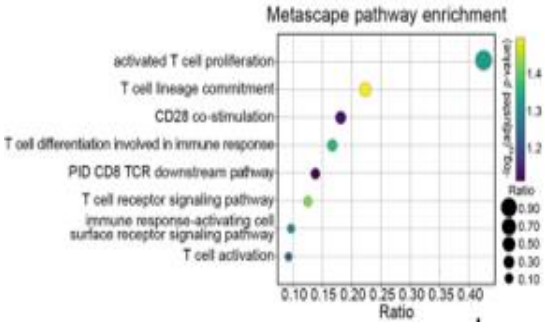

g)

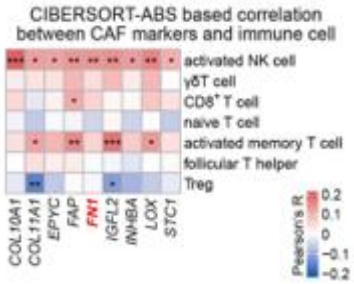

h)

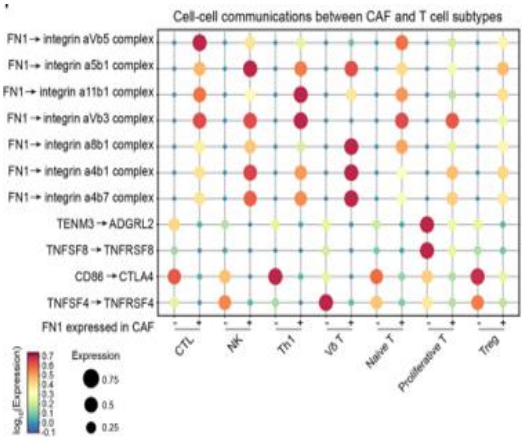

i)

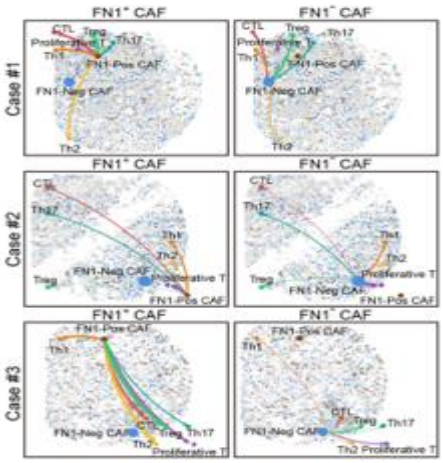

j)

Figure 7. ZFP36 restricts FN1-expressing CAF support of T-cell activation via mRNA destabilization in H. pylori-driven gastric cancer. **a** Conceptual diagram of ZFP36 function. The figure illustrates ZFP36 recognition of AU-rich (AUUUA) sequences in 3′UTRs leading to transcript degradation. **b** Scatter diagram ranking genes by Pearson correlation to ZFP36 and ATTTA motif density in their 3′UTRs as indicators of canonical ARE presence. Candidates meeting Pearson's R < -0.2 and ≥ 5 ATTTA motifs are marked. **c** Circos display of GO terms enriched in forecasted ZFP36 targets within CAFs. Immune processes and cytokine pathways rank highly. **d** UMAP expression overlays for ZFP36 and chosen immune-relevant genes in CAF clusters. **e** Scatter representation of inversely correlated genes ordered by correlation magnitude and significance against ZFP36. **f** Circos view of ZFP36 enrichment sites along the FN1 gene from LACE-seq across four replicates (#1-#4). The transcription start site (TSS) is marked, with sample-specific peaks shown as colored segments. **g** Bubble chart of pathway enrichment for ZFP36-linked targets via Metascape. Bubble diameter denotes gene coverage, and the color gradient reflects adjusted P-values. **h** Heatmap of Pearson correlations linking selected CAF signatures to immune subsets via CIBERSORT-ABS deconvolution. Color scale shows coefficients, asterisks denote significance (*P < 0.05; **P < 0.01; ***P < 0.001). **i** Bubble chart of forecasted ligand-receptor pairs between FN1$^+$/FN1$^-$ CAFs and T-cell categories. Circle size indicates interaction intensity, and color encodes log10 expression. **j** Tissue-resolved signaling networks contrasting FN1$^+$ versus FN1$^-$ CAFs in example gastric cancer sections. Arced connections depict anticipated crosstalk with T-cell populations, positioned within individual samples.

To further characterize the regulatory landscape of ZFP36-expressing CAFs, we performed single-cell regulon inference using the SCENIC pipeline to estimate transcription factor activity. UMAP projections showed that ZFP36-high CAFs were dominated by regulons driven by ATF3, JUN, and FOS, which are known mediators of stress responses and inflammatory signaling. This suggests that ZFP36 operates within a broader stress-activated transcriptional network to shape the immune-suppressive properties of CAFs. Supporting this, functional enrichment of ZFP36-repressed targets pointed to strong involvement in T-cell activation and co-stimulation pathways **(Figure 7g)**. To assess the functional impact of FN1 suppression, we correlated bulk FN1 levels with immune infiltration via CIBERSORT-ABS. High FN1 in the stromal compartment was strongly linked to increased abundance of several effector T-cell populations, especially activated CD8$^+$ and γδ T cells **(Figure 7h)**. Refining the T-cell landscape, we resolved seven transcriptionally unique T-cell clusters. Ligand-receptor inference indicated that FN1$^+$ CAFs established far more extensive connections with T cells than FN1$^-$ CAFs, primarily through integrin complexes and immune-checkpoint axes such as α5β1-FN1, CD86-CTLA4, and TNFSF4-TNFRSF4 **(Figure 7i)**. Spatial interaction networks confirmed that FN1$^+$ CAFs displayed markedly stronger local engagement with cytotoxic T-cell subsets, including CTLs, across tumor sections compared with FN1$^-$ CAFs **(Figure 7j)**.

Together, these data show that ZFP36-mediated destabilization of FN1 mRNA disables a pro-activating CAF program that normally supports cytotoxic T-cell function, thereby reinforcing immunosuppression in H. pylori-driven gastric cancer.

In the present work, we combined spatial transcriptomics with single-cell RNA sequencing to produce a detailed atlas of the cancer-associated fibroblast (CAF) compartment in gastric cancer (GC). By delineating CAF subpopulations, mapping their tissue distribution, and reconstructing their differentiation paths, we uncovered previously unrecognized mechanisms by which specific CAF subsets orchestrate immune evasion, especially in H. pylori-positive tumors. In particular, THBS1$^+$ and ZFP36$^+$ CAFs emerged as central players that jointly promote an immunosuppressive niche by enhancing regulatory T-cell accumulation and simultaneously blocking effective cytotoxic responses. These observations position these two CAF populations as critical stromal nodes linking chronic H. pylori infection to tumor immune escape and disease progression.

The tumor microenvironment (TME) is a major determinant of GC behavior and therapeutic response [28]. Within the stromal compartment, CAFs are now acknowledged as active architects of tumor progression, immune regulation, and matrix reorganization [29, 30]. We documented profound histological differences in spatial architecture: intestinal-type tumors displayed tightly packed malignant epithelial regions with CAFs and immune cells confined to the invasive front, creating clear tumor–stroma interfaces; diffuse-type tumors, conversely, exhibited chaotic interspersion of cancer cells, fibroblasts, and leukocytes, mirroring their poorly cohesive phenotype. Spatial aggregation metrics confirmed significantly stronger tumor-cell clustering in intestinal-type cases. These patterns align with the traditional Lauren classification and establish a structural basis for subtype-specific stromal–immune dynamics [7, 31]. Beyond anatomy, intercellular signaling analysis showed that intestinal-type tumors retained more organized and polarized communication networks, whereas diffuse-type tumors had reduced dendritic-cell output, weaker T-cell circuits, and scattered fibroblast–immune signaling, suggestive of impaired immune surveillance. These results reinforce earlier evidence of histology-dependent immune regulation in GC [32, 33] and indicate that diffuse-type tumors may evade immunity partly through disrupted signaling architecture.

Although inflammatory CAFs (iCAFs) were the subpopulation located closest to malignant cells and displayed the most active stromal–immune crosstalk, the infection-responsive genes ZFP36 and THBS1 were primarily upregulated in progenitor CAFs (proCAFs). This apparent paradox likely reflects the temporal dynamics of H. pylori-triggered stromal activation. As the earliest CAF precursors, proCAFs are probably the first fibroblasts to sense infection-driven inflammatory cues, rapidly acquiring immunosuppressive features (ZFP36- and THBS1-dependent programs) that establish immune tolerance during the pre-neoplastic and early neoplastic phases. Our prior research indicated that large-scale iCAF expansion occurs downstream of proCAF induction and leads to their accumulation around established tumor nests [18]. Thus, proCAFs serve as the initial infection-sensing compartment that installs suppressive machinery, whereas iCAFs represent a later amplification stage that physically surrounds cancer cells and sustains the immunosuppressive environment. This model provides a spatiotemporal framework for how sequential CAF subsets cooperate to entrench immune evasion during H. pylori-associated gastric carcinogenesis.

Helicobacter pylori is a well-documented inducer of tumor-promoting inflammation and stromal remodeling in GC. Here, we observed a substantial rise in CAF fraction in H. pylori-positive tumors, recapitulating earlier reports, including our own demonstration that H. pylori activates the NF-κB/PIEZO1/YAP1/CTGF cascade to recruit CAFs, reorganize the extracellular matrix, and foster an immunosuppressive milieu [14]. Complementary studies have further shown that H. pylori triggers CAF conversion from normal fibroblasts through cytokines such as Serpin E1, thereby accelerating tumor growth and neovascularization [34, 35]. Taken together, these data cement H. pylori as a master regulator of CAF phenotypic switching, spatial deployment, and immune-suppressive specialization, illuminating the mechanistic chain from chronic infection to stromal-mediated disease progression in gastric cancer.

At the mechanistic level, our investigation revealed two prominent molecules, THBS1 and ZFP36, that showed marked upregulation in cancer-associated fibroblasts from Helicobacter pylori-infected gastric tumors. Notably, higher levels of these genes correlated robustly with unfavorable patient outcomes, evidenced by substantially reduced overall survival among cases with prominent THBS1$^+$/ZFP36$^+$ CAF populations. Regarding

THBS1, its distribution overlapped with zones rich in regulatory T cells, implying involvement in Treg attraction. Considering its established ability to trigger TGF-β pathways and impair T-cell responses through the CD47-SIRPα interaction [36, 37], THBS1-expressing CAFs probably play a major role in creating a suppressive immune setting. Remarkably, individuals displaying THBS1$^+$ CAFs alongside minimal Treg clustering achieved roughly double the survival duration relative to those with extensive Treg aggregation, emphasizing the biological importance of this association. To uncover the mediating pathway, we evaluated forecasted intercellular signaling and pinpointed WNT-FZD connections as the primary route linking THBS1$^+$ CAFs to Tregs. Although not a typical migratory signal, WNT pathways are recognized for sustaining Treg populations and blocking dendritic cell development to favor tolerance [38, 39]. This evidence supports a scenario where a THBS1-WNT pathway drives Treg buildup and immunosuppressive compartment formation in H. pylori-linked gastric cancer. On a parallel track, the AU-rich element-recognizing protein ZFP36 could influence CAF-dependent immunity via an independent route [40, 41]. Our data indicated a clear inverse relationship between ZFP36 levels and FN1, an essential matrix protein formerly tied to immune barrier formation through increased stiffness and obstacles to T-cell entry [42, 43]. Intriguingly, spatial crosstalk mapping displayed an opposing trend: FN1$^+$ CAFs showed greater proximity to cytotoxic T lymphocytes and natural killer cells, while FN1$^-$ CAFs aligned more with Treg contacts. Such patterns imply that, within H. pylori-driven gastric cancer, FN1 might support immune stimulation, possibly by facilitating contacts with effector cytotoxic populations [44, 45]. Accordingly, ZFP36 likely dampens pro-immune CAF traits by reducing FN1 expression, thus reinforcing THBS1 effects through a complementary control mechanism to sustain immunosuppression.

Overall, our combined spatial and molecular characterization establishes THBS1$^+$ and ZFP36$^+$ CAFs as principal coordinators of immune suppression and adverse prognosis in H. pylori-positive gastric cancer. In particular, the THBS1-WNT5 pathway seems to enhance Treg accumulation and persistence, while the ZFP36-FN1 pathway governs immune barrier effects and cytotoxic cell engagement, jointly fostering a non-inflammatory ("cold") tumor ecosystem. Nonetheless, these interpretations rely predominantly on expression associations and await experimental confirmation. Upcoming research employing targeted disruption of these genes in CAFs and animal models, altering THBS1 and ZFP36 function, will be essential to prove direct causality in immune regulation. Such knowledge could justify stromal-focused interventions to augment immunotherapy in H. pylori-related gastric cancer.

Conclusion

In summary, this work maps the positional and functional diversity of CAF subpopulations in gastric cancer and positions H. pylori infection as a major environmental modulator of CAF immune-regulatory properties. We describe two separate CAF-orchestrated immunosuppressive loops—the THBS1-WNT5-Treg circuit and the ZFP36-FN1 axis—that together promote a tolerant tumor microenvironment in infection-driven cases. These discoveries yield fresh understanding of stromal–immune–malignant cell dynamics and suggest potential for CAF-directed approaches in upcoming immune-based treatments.

Acknowledgments: None

Conflict of Interest: None

Financial Support: None

Ethics Statement: None

References

1. Smyth EC, Nilsson M, Grabsch HI, van Grieken NC, Lordick F: Gastric cancer. Lancet. 2020;96:635–648.
2. Duan Y, Xu Y, Dou Y, Xu D:Helicobacter pylori and gastric cancer: mechanisms and new perspectives. J Hematol Oncol. 2025,18:10.
3. Zeng R, Gou H, Lau HCH, Yu J: Stomach microbiota in gastric cancer development and clinical implications. Gut. 2024;73:2062–2073.
4. Huang J, Lucero-Prisno DE, 3rd, Zhang L, Xu W, Wong SH, Ng SC, Wong MCS: Updated epidemiology of gastrointestinal cancers in East Asia. Nat Rev Gastroenterol Hepatol. 2023;20:271–87.

5. Wang SN, Yun T, Zhu CY, Li P, Ge DF, Li SL, Wang YK: Immune cell changes in Helicobacter pylori infection-induced glandular epithelial cell damage of the gastric mucosa. Ann Med. 2024;56:2425072.
6. Wu M-S, Shun C-T, Wang H-P, Sheu J-C, Lee W-J, Wang T-H, Lin J-T: Genetic alterations in gastric cancer: relation to histological subtypes, tumor stage, and Helicobacter pylori infection. Gastroenterology. 1997;112:1457–65.
7. Chia NY, Tan P: Molecular classification of gastric cancer. Ann Oncol. 2016;27:763–9.
8. Lin Y, Pan X, Zhao L, Yang C, Zhang Z, Wang B, Gao Z, Jiang K, Ye Y, Wang S, Shen Z: Immune cell infiltration signatures identified molecular subtypes and underlying mechanisms in gastric cancer. NPJ Genom Med. 2021;6:83.
9. Lv C, Chen T, Li J, Shan Y, Zhou H: A comprehensive analysis of molecular characteristics of hot and cold tumor of gastric cancer. Cancer Immunol Immunother. 2025;74:102.
10. Parsonnet J, Vandersteen D, Goates J, Sibley RK, Pritikin J, Chang Y: Helicobacter pylori infection in intestinal- and diffuse-type gastric adenocarcinomas. J Natl Cancer Inst. 1991;83:640–3.
11. Cristescu R, Lee J, Nebozhyn M, Kim KM, Ting JC, Wong SS, Liu J, Yue YG, Wang J, Yu K, et al: Molecular analysis of gastric cancer identifies subtypes associated with distinct clinical outcomes. Nat Med. 2015;21:449–56.
12. Sohn BH, Hwang JE, Jang HJ, Lee HS, Oh SC, Shim JJ, Lee KW, Kim EH, Yim SY, Lee SH, et al: Clinical Significance of Four Molecular Subtypes of Gastric Cancer Identified by The Cancer Genome Atlas Project. Clin Cancer Res. 2017;23:4441–9.
13. Krzysiek-Maczka G, Targosz A, Szczyrk U, Strzałka M, Sliwowski Z, Brzozowski T, Czyz J, Ptak-Belowska A: Role of Helicobacter pylori infection in cancer-associated fibroblast-induced epithelial-mesenchymal transition in vitro. Helicobacter. 2018;23:e12538.
14. Chen B, Liu X, Yu P, Xie F, Kwan JSH, Chan WN, Fang C, Zhang J, Cheung AHK, Chow C, et al: H. pylori-induced NF-κB-PIEZO1-YAP1-CTGF axis drives gastric cancer progression and cancer-associated fibroblast-mediated tumour microenvironment remodelling. Clin Transl Med. 2023;13:e1481.
15. Mak TK, Li X, Huang H, Wu K, Huang Z, He Y, Zhang C: The cancer-associated fibroblast-related signature predicts prognosis and indicates immune microenvironment infiltration in gastric cancer. Front Immunol. 2022;13:951214.
16. Sun H, Wang X, Wang X, Xu M, Sheng W: The role of cancer-associated fibroblasts in tumorigenesis of gastric cancer. Cell Death Dis. 2022;13:874.
17. Yao L, Hou J, Wu X, Lu Y, Jin Z, Yu Z, Yu B, Li J, Yang Z, Li C, et al: Cancer-associated fibroblasts impair the cytotoxic function of NK cells in gastric cancer by inducing ferroptosis via iron regulation. Redox Biol. 2023;67:102923.
18. Chen B, Chan WN, Xie F, Mui CW, Liu X, Cheung AHK, Lung RWM, Chow C, Zhang Z, Fang C, et al: The molecular classification of cancer-associated fibroblasts on a pan-cancer single-cell transcriptional atlas. Clin Transl Med. 2023;13:e1516.
19. Ståhl PL, Salmén F, Vickovic S, Lundmark A, Navarro JF, Magnusson J, Giacomello S, Asp M, Westholm JO, Huss M, et al: Visualization and analysis of gene expression in tissue sections by spatial transcriptomics. Science. 2016;353:78–82.
20. Jain S, Rick JW, Joshi RS, Beniwal A, Spatz J, Gill S, Chang AC, Choudhary N, Nguyen AT, Sudhir S, et al: Single-cell RNA sequencing and spatial transcriptomics reveal cancer-associated fibroblasts in glioblastoma with protumoral effects. J Clin Invest. 2023:133.
21. Wang Z, Wang Q, Chen C, Zhao X, Wang H, Xu L, Fu Y, Huang G, Li M, Xu J, et al: NNMT enriches for AQP5(+) cancer stem cells to drive malignant progression in early gastric cardia adenocarcinoma. Gut. 2023;73:63–77.
22. Sathe A, Grimes SM, Lau BT, Chen J, Suarez C, Huang RJ, Poultsides G, Ji HP: Single-Cell Genomic Characterization Reveals the Cellular Reprogramming of the Gastric Tumor Microenvironment. Clin Cancer Res. 2020;26:2640–53.
23. Kumar V, Ramnarayanan K, Sundar R, Padmanabhan N, Srivastava S, Koiwa M, Yasuda T, Koh V, Huang KK, Tay ST, et al: Single-Cell Atlas of Lineage States, Tumor Microenvironment, and Subtype-Specific Expression Programs in Gastric Cancer. Cancer Discov. 2022;12:670–91.
24. He S, Bhatt R, Brown C, Brown EA, Buhr DL, Chantranuvatana K, Danaher P, Dunaway D,

Garrison RG, Geiss G, et al: High-plex imaging of RNA and proteins at subcellular resolution in fixed tissue by spatial molecular imaging. Nat Biotechnol. 2022;40:1794–1806.

25. Setty M, Kiseliovas V, Levine J, Gayoso A, Mazutis L, Pe'Er D: Characterization of cell fate probabilities in single-cell data with Palantir. Nature biotechnology. 2019;37:451–60.
26. Cancer Genome Atlas Research Network. Comprehensive molecular characterization of gastric adenocarcinoma. Nature 2014, 513:202–209.
27. Zhou Y, Zhou B, Pache L, Chang M, Khodabakhshi AH, Tanaseichuk O, Benner C, Chanda SK: Metascape provides a biologist-oriented resource for the analysis of systems-level datasets. Nat Commun. 2019;10:1523.
28. Zhou Y, Zhou B, Pache L, Chang M, Khodabakhshi AH, Tanaseichuk O, Benner C, Chanda SK: Metascape provides a biologist-oriented resource for the analysis of systems-level datasets. Nat Commun. 2019;10:1523.
29. Song J, Wei R, Liu C, Zhao Z, Liu X, Wang Y, Liu F, Liu X: Antigen-presenting cancer associated fibroblasts enhance antitumor immunity and predict immunotherapy response. Nat Commun. 2025;16:2175.
30. Rimal R, Desai P, Daware R, Hosseinnejad A, Prakash J, Lammers T, Singh S: Cancer-associated fibroblasts: Origin, function, imaging, and therapeutic targeting. Adv Drug Deliv Rev. 2022;189:114504.
31. Pernot S, Terme M, Radosevic-Robin N, Castan F, Badoual C, Marcheteau E, Penault-Llorca F, Bouche O, Bennouna J, Francois E: Infiltrating and peripheral immune cell analysis in advanced gastric cancer according to the Lauren classification and its prognostic significance. Gastric Cancer. 2020;23:73–81.
32. Zeng D, Li M, Zhou R, Zhang J, Sun H, Shi M, Bin J, Liao Y, Rao J, Liao W: Tumor Microenvironment Characterization in Gastric Cancer Identifies Prognostic and Immunotherapeutically Relevant Gene Signatures. Cancer Immunol Res. 2019;7:737–750.
33. Zhou Y, Li J: Immunotherapy for diffuse gastric cancer: challenges and new avenues. NPJ Precis Oncol. 2025;9:247.
34. Chen X, Chen W, Zhao Y, Wang Q, Wang W, Xiang Y, Yuan H, Xie Y, Zhou J: Interplay of Helicobacter pylori, fibroblasts, and cancer cells induces fibroblast activation and serpin E1 expression by cancer cells to promote gastric tumorigenesis. J Transl Med. 2022;20:322.
35. Krzysiek-Maczka G, Brzozowski T, Ptak-Belowska A: Helicobacter pylori-activated fibroblasts as a silent partner in gastric cancer development. Cancer Metastasis Rev. 2023;42:1219–56.
36. Omatsu M, Nakanishi Y, Iwane K, Aoyama N, Duran A, Muta Y, Martinez-Ordoñez A, Han Q, Agatsuma N, Mizukoshi K, et al: THBS1-producing tumor-infiltrating monocyte-like cells contribute to immunosuppression and metastasis in colorectal cancer. Nat Commun. 2023;14:5534.
37. Li J, Feng H, Zhu J, Yang K, Zhang G, Gu Y, Shi T, Chen W: Gastric cancer derived exosomal THBS1 enhanced Vγ9Vδ2 T-cell function through activating RIG-I-like receptor signaling pathway in a N6-methyladenosine methylation dependent manner. Cancer Letters. 2023;576:216410.
38. Wang J, Zhao X, Wan YY: Intricacies of TGF-β signaling in Treg and Th17 cell biology. Cell Mol Immunol. 2023;20:1002–22.
39. van Loosdregt J, Fleskens V, Tiemessen MM, Mokry M, van Boxtel R, Meerding J, Pals CE, Kurek D, Baert MR, Delemarre EM, et al: Canonical Wnt signaling negatively modulates regulatory T cell function. Immunity. 2013;39:298–310.
40. Cook ME, Bradstreet TR, Webber AM, Kim J, Santeford A, Harris KM, Murphy MK, Tran J, Abdalla NM, Schwarzkopf EA, et al: The ZFP36 family of RNA binding proteins regulates homeostatic and autoreactive T cell responses. Sci Immunol. 2022;7:eabo0981.
41. Sáenz-Narciso B, Bell SE, Matheson LS, Venigalla RK, Turner M: ZFP36-family RNA-binding proteins in regulatory T cells reinforce immune homeostasis. Nature Communications. 2025;16:1–20.
42. Spada S, Tocci A, Di Modugno F, Nisticò P: Fibronectin as a multiregulatory molecule crucial in tumor matrisome: from structural and functional features to clinical practice in oncology. J Exp Clin Cancer Res. 2021;40:102.
43. Pan S, Zhu J, Liu P, Wei Q, Zhang S, An W, Tong Y, Cheng Z, Liu F: FN1 mRNA 3'-UTR supersedes traditional fibronectin 1 in facilitating the invasion and metastasis of gastric cancer through the FN1 3'-UTR-let-7i-5p-THBS1 axis. Theranostics. 2023;13:5130–150.

44. Efthymiou G, Saint A, Ruff M, Rekad Z, Ciais D, Van Obberghen-Schilling E: Shaping Up the Tumor Microenvironment With Cellular Fibronectin. Front On. 2020;10:641.

45. Lin TC, Yang CH, Cheng LH, Chang WT, Lin YR, Cheng HC: Fibronectin in Cancer: Friend or Foe. Cells. 2019;9:27.